

## 3D fold growth in transpression

Marcel Frehner\*

Geological Institute, ETH Zurich, Sonneggstrasse 5, Switzerland



### ARTICLE INFO

#### Article history:

Received 14 July 2015

Received in revised form 25 November 2015

Accepted 4 January 2016

Available online 13 January 2016

#### Keywords:

Buckle folds

Transpression

Fold growth

Hinge migration

Fold rotation

Zagros fold-and-thrust-belt

### ABSTRACT

Geological folds in transpression are inherently 3D structures; hence their growth and rotation behavior is studied using 3D numerical finite-element simulations. Upright single-layer buckle folds in Newtonian materials are considered, which grow from an initial point-like perturbation due to a combination of in-plane shortening and shearing (i.e., transpression). The resulting fold growth exhibits three components: (1) fold amplification (vertical), (2) fold elongation (parallel to fold axis), and (3) sequential fold growth (perpendicular to axial plane) of new anti- and synforms adjacent to the initial fold. Generally, the fold growth rates are smaller for shearing-dominated than for shortening-dominated transpression. In spite of the growth rate, the folding behavior is very similar for the different convergence angles. The two lateral directions always exhibit similar growth rates implying that the bulk fold structure occupies an increasing roughly circular area. Fold axes are always parallel to the major horizontal principal strain axis ( $\vec{\lambda}_{\max}$ , i.e., long axis of the horizontal finite strain ellipse), which is initially also parallel to the major horizontal instantaneous stretching axis ( $\vec{I\bar{S}A}_{\max}$ ). After initiation, the fold axes rotate together with  $\vec{\lambda}_{\max}$ . Sequential folds appearing later do not initiate parallel to  $\vec{I\bar{S}A}_{\max}$ , but parallel to  $\vec{\lambda}_{\max}$ , i.e. parallel to the already existing folds, and also rotate with  $\vec{\lambda}_{\max}$ . Therefore, fold axes do not correspond to passive material lines and hinge migration takes place as a consequence. The fold axis orientation parallel to  $\vec{\lambda}_{\max}$  is independent of convergence angle and viscosity ratio. Therefore, a triangular relationship between convergence angle, amount of shortening, and fold axis orientation exists. If two of these values are known, the third can be determined. This relationship is applied to the Zagros fold-and-thrust-belt to estimate the degree of strain partitioning between the Simply Folded Belt and the bordering strike-slip fault-system.

© 2016 Elsevier B.V. All rights reserved.

### 1. Introduction

Transpression, or oblique convergence, is a common tectonic setting at plate boundaries characterized by two components of relative plate velocity (Sanderson and Marchini, 1984): one component is perpendicular to the plate boundary (i.e., shortening component) and one component is parallel to the plate boundary (i.e., strike-slip component). Examples of transpressional tectonic settings can be found in oblique subduction systems, such as on the South Island of New Zealand (Teyssier et al., 1995; Toy et al., 2013), in Sumatra (Tikoff and Teyssier, 1994), or in the Argentinian and Chilean Andes (Lupi and Miller, 2014; Payrola et al., 2012), at restraining bends of strike-slip faults, such as the Big Bend in the San Andreas Fault (Kellogg and Minor, 2005; Teyssier et al., 1995; Tikoff and Teyssier, 1994), and in continent-continent collision zones, such as in parts of the Swiss Alps (Dewey et al., 1998) or in the collision zone between the Arabian and Eurasian continental plates. For the last mentioned tectonic system, the convergence angle (angle between relative velocity vector and plate boundary) decreases from 70° in the Caucasus area (Jackson, 1992) to 45° in the

western Iranian Zagros Simply Folded Belt (Vernant and Chéry, 2006) and to 25° in the south-western Iranian Fars area (Sarkarinejad, 2007) and the Sanandaj-Sirjan Zone (Mohajjel and Fergusson, 2000).

Transpression has been described in detail using kinematical homogeneous-strain models (Fossen and Tikoff, 1993; Fossen et al., 2013; Sanderson and Marchini, 1984). However, transpressional systems can exhibit strain partitioning resulting in domains of simple-shear dominated structures and domains of shortening-dominated structures (see Talebian and Jackson, 2004 and Vernant and Chéry, 2006 for an application to the Zagros Mountains). The kinematical homogeneous-strain models have been extended to such systems to include a heterogeneous (i.e., partitioned) strain distribution (Jones and Tanner, 1995; Tikoff and Teyssier, 1994). However, Robin and Cruden (1994) and later Dewey et al. (1998) demonstrated that transpressional systems and related strain partitioning can lead to very complex foliation and lineation patterns, which may not be explained by one single kinematical model.

The present study focusses on folds developing in transpressional tectonic settings. Geological folds are inherently 3D structures; hence their growth ideally has to be investigated as a 3D process, which has been done analytically (Fletcher, 1995, 1991; Ghosh, 1970; Mühlhaus et al., 1998), in laboratory experiments (Abbassi and Mancktelow,

\* Tel.: +41 44 632 5468; fax: +41 44 632 1030.  
E-mail address: [marcel.frehner@erdw.ethz.ch](mailto:marcel.frehner@erdw.ethz.ch).

1992; Zulauf et al., 2003), and numerically (Fernandez and Kaus, 2014; Frehner, 2014; Grasmann and Schmalholz, 2012; Kaus and Schmalholz, 2006; Schmid et al., 2008). However, the vast majority of such studies only considered uni- or bi-directional shortening (co-axial) boundary conditions. Transpression has been studied far less.

One of the major questions for folding studies in transpression is how folds are oriented with respect to the background velocity vector. It is generally agreed that during the earliest folding stages, the fold axis initiates parallel to the major horizontal instantaneous stretching axis,  $\vec{\lambda}_{\max}$  (Fossen et al., 2013; James and Watkinson, 1994; Tikoff and Peterson, 1998; Treagus and Treagus, 1981). However, Fossen et al. (2013) stated that: “Exactly how fold elements (axis, axial plane) rotate after initiation is not clear”. A small number of analog laboratory experiments investigated fold growth in transpression. Payrola et al. (2012) mimicked oblique fold structures in northwestern Argentina in transpressional analog experiments with a convergence angle of 55°; yet the fold axis orientation was not tracked during deformation. Casas et al. (2001) modeled general transpression (convergence angle 0°–90°) above a linear velocity discontinuity at the base of their modeling box. Folds developed due to passive bulging related to thrusts originating from this imposed discontinuity. Therefore, the folds were always parallel to the discontinuity and no systematic study on fold orientation was conducted. Leever et al. (2011) modeled a transpressional system in Spitzbergen, which exhibits a convergence angle of 15°. They also used a basal velocity discontinuity, yet their model was large enough to allow folds to develop away from and independently of this discontinuity. This allowed them to track the fold orientation during deformation and to identify a significant rotation of the fold axis after fold initiation. However, they did not link this rotation to any kinematical model. Similarly, Ghosh et al. (2014) observed fold axis rotation after fold initiation, but also did not link it to a kinematical model. Tikoff and Peterson (1998) modeled folds in general transpression with the particular aim of tracking the fold axis orientation. They found that the fold axis is always parallel to the major horizontal principal strain axis,  $\vec{\lambda}_{\max}$ ; that means it initiates in this direction and rotates together with this orientation. At the same time, Grujic and Mancktelow (1995) performed similar experiments, but only in simple shear (convergence angle 0°), and found that the fold axis rotates as a passive line fixed to the material. The findings of Tikoff and Peterson (1998) imply the occurrence of hinge migration during deformation (i.e., the fold hinge migrates through the material) while the findings of Grujic and Mancktelow (1995) exclude hinge migration. Fossen et al. (2013) suggested that: “More data from physical experiments, numerical modeling and field observations are needed to further explore this question”. This is the primary aim of this study.

The presented work is an extension and generalization of the numerical modeling work presented in Frehner (2014), which only considered 3D folding under pure shortening (convergence angle 90°). After the definition of 3D fold growth, the numerical model with its initial and boundary conditions is outlined and the methods to track fold amplitudes and orientations during deformation are explained. The results are divided into a fold orientation-independent part and a part particularly focusing on the fold axis rotation and related hinge migration. In the discussion section, the fold axis orientation data from the analog experiments of Leever et al. (2011) is reevaluated and linked to the kinematical model established before. This kinematical model is then applied to the Iraqi Zagros fold-and-thrust-belt, which represents a natural transpressional system, to estimate the degree of strain partitioning between the Simply Folded Belt and the bordering strike-slip fault system.

### 1.1. Definition of fold growth in 3D

For transpression, the fold growth definitions in 3D given in Frehner (2014) have to be slightly modified. Using the coordinate

system in Fig. 1, fold growth in 3D exhibits the following three components:

- Fold amplification: Growth from a fold shape with low limb-dip angle to a shape with larger limb-dip angle. In the presented cases, fold amplification corresponds to the growth in z-direction (vertical).
- Fold elongation: Growth parallel to fold axis from a dome-shaped (3D) structure to a more cylindrical (2D) structure. In the case of pure-shear background deformation, fold elongation corresponds to the growth in x-direction.
- Sequential fold growth: Growth perpendicular to fold axial plane of additional folds adjacent to the initial isolated fold. The initial fold is termed the 0<sup>th</sup> sequential fold; later grown folds are numbered accordingly. In the case of pure-shear background deformation, sequential fold growth corresponds to the growth in y-direction.

## 2. Numerical method and setup

Buckle folding is assumed to be a quasi-static flow process in the absence of gravity governed by incompressible Newtonian (linear viscous) rheology. The corresponding continuum mechanics equations describing such flow behavior are described in Appendix A; their discretization with the finite-element (FE) method is described in Appendix B. The entire model is non-dimensionalized using three pre-defined characteristic values:

- Characteristic length scale: Initial thickness of the top layer,  $H_L$
- Characteristic time scale: Inverse of background strain rate,  $1/\dot{\epsilon}_{bg}$
- Characteristic viscosity scale: Viscosity of the lower (matrix) layer,  $\eta_M$

Due to this non-dimensionalization, the obtained results may not be translated one-to-one to natural cases, but must first be back-dimensionalized using real values for the three characteristic scales.

### 2.1. Model setup and boundary conditions

The model setup and boundary conditions are depicted in Fig. 1. The model is centered at ( $x = 0, y = 0$ ) and consists of two layers, an upper layer with higher viscosity (thickness  $H_L = 1$ , viscosity  $\eta_L$ ) resting on top of a lower-viscosity (matrix) layer (thickness  $H_M$ , viscosity  $\eta_M = 1$ , viscosity ratio  $R = \eta_L/\eta_M$ ). The thickness of the lower layer is large enough to fall into the domain of matrix-controlled folding ( $\frac{H_M}{H_L} \gg \frac{4}{3}(\frac{2}{3}R)^{1/3}$ ; Schmalholz et al., 2002); hence the exact value of  $H_M$  does not influence the results.

The following boundary conditions are applied to enforce general transpression with convergence angle  $\alpha$  (Fig. 1):

- Top boundary: Free surface boundary conditions.
- Bottom boundary: Non-moving free-slip boundary conditions (i.e., zero traction, zero boundary-perpendicular velocity).
- All lateral boundaries: The velocity components in the x- and y-directions are enforced according to

$$v_x = y\dot{\epsilon}_{bg} \cos(\alpha), \quad (1)$$

$$v_y = -y\dot{\epsilon}_{bg} \sin(\alpha), \quad (2)$$

where  $y$  represents the y-coordinate values of the corresponding boundaries. Consequently, both velocity components are modified at every time step during a simulation to maintain the externally applied constant background strain rate,  $\dot{\epsilon}_{bg} = 1$  (a positive value). In the z-direction, free slip boundary conditions are applied.

This set of boundary conditions corresponds to simple shear (wrenching) with the shear plane perpendicular to the y-axis and the

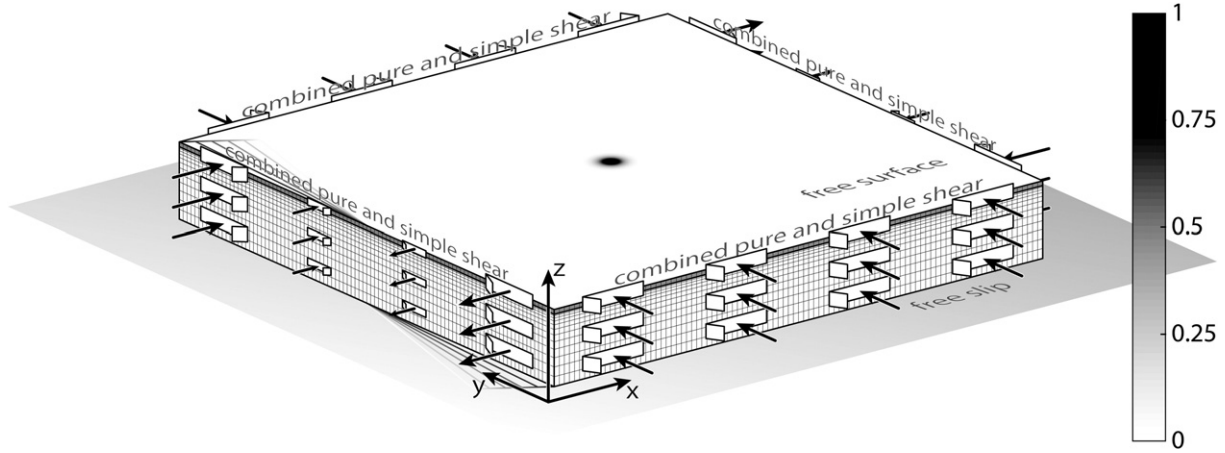


**Fig. 1.** Initial model setup, boundary conditions, and coordinate system used in this study. The model is centered at  $(x = 0, y = 0)$ . The two-layer model comprises a top layer with higher viscosity resting on a (matrix) layer with lower viscosity. Transpressional boundary conditions are applied at all lateral boundaries as a combination of boundary-perpendicular (black arrows) and boundary-parallel (white arrows) velocity components; smaller arrows represent smaller applied velocity values. Gray levels represent the initial Gaussian topography measured in per cent of the thickness of the top layer. The diminishing gray lines at the left edge of the model indicate progressive deformation of this edge in the case of general transpression.

shear direction parallel to the x-axis for  $\alpha = 0^\circ$  (Frehner et al., 2011), to pure shear (pure shortening) with shortening parallel to the y-axis and extension parallel to the z-axis for  $\alpha = 90^\circ$  (Frehner, 2014), and to general transpression for a general convergence angle,  $0^\circ < \alpha < 90^\circ$ , which is a combination of the two end-member cases. Exactly the same boundary conditions are considered in Sanderson and Marchini (1984) and Fossen et al. (2013) and mimicked in the analog experiments of Grujic and Mancktelow (1995) and Tikoff and Peterson (1998). The convergence angle also provides the orientation of the flow apophysis in top view, which is not parallel to the shear plane (Fossen et al., 2013). The kinematic vorticity number may be calculated as  $W_k = \cos(\alpha)$  (Bobyarchick, 1986); yet, the convergence angle,  $\alpha$ , is used throughout this study.

A point-like initial perturbation,  $G$ , is superposed onto both the top and bottom interface of the upper layer in the shape of a 2D Gaussian (Fig. 1),

$$G = A_0 \exp\left(\frac{x^2}{2\sigma^2}\right) \exp\left(\frac{y^2}{2\sigma^2}\right), \quad (3)$$

with a small initial amplitude of  $A_0 = 0.01$  (1% of the upper layer thickness). This initial perturbation forces the mechanical folding instability to initialize and grow from the center of the model, which allows quantifying fold growth in transpression away from any possible boundary effects. The effective wavelength of the initial perturbation is defined as

$$\lambda_0 = 2 \times \text{FWHM} = 2 \times \sqrt{8 \ln(2)}\sigma, \quad (4)$$

where FWHM is the full width at half maximum of the 2D Gaussian. According to Frehner (2014), the effective initial wavelength,  $\lambda_0$ , is equal to the dominant wavelength (Fletcher, 1991) by setting  $\sigma = 6$  for  $R = 100$  and by setting  $\sigma = 4$  for  $R = 20$ ; hence these values ( $R = 100, \sigma = 6$  and  $R = 20, \sigma = 4$ ) are set constant in the presented study.

### 2.2. Background strain measure

To compare simulations with different convergence angles, there is no unique bulk strain measure for general transpression. Appendix C presents some possibilities for measuring the bulk strain and discusses their advantages and disadvantages. Based on these considerations,

the background strain,  $\epsilon_{bg}$ , is proposed here as a global measure for all convergence angles:

$$\epsilon_{bg} = 1 - \exp(-t\dot{\epsilon}_{bg}), \quad (5)$$

where  $t$  is time and  $\dot{\epsilon}_{bg}$  is the externally applied background strain rate. This background strain measure is used throughout the study. However, Table 1 translates  $\epsilon_{bg}$ -values to the lengths of the minor ( $|\vec{\lambda}_{min}|$ ) and major ( $|\vec{\lambda}_{max}|$ ) horizontal principal strain axes, respectively. The former is the only other strain measure identified in Appendix C as being suitable for all convergence angles. Here,  $\vec{\lambda}_{min}$  and  $\vec{\lambda}_{max}$  are written as vectors, indicating that they represent both a length (1 plus the strain value) and an orientation (the strain axis orientation).

**Table 1**

Translation from background strain ( $\epsilon_{bg}$ ) values given in Figs. 2, 3, and 8 to the lengths of the minor ( $|\vec{\lambda}_{min}|$ ) and major ( $|\vec{\lambda}_{max}|$ ) horizontal principal strain axes (rounded to two digits after decimal point).

| Convergence angle                  | Fig. 3   |  |  | Fig. 8   | Fig. 2 |
|------------------------------------|--|--|--|--|--------|
|                                    | 1 <sup>st</sup> snapshot   | 2 <sup>nd</sup> snapshot   | 3 <sup>rd</sup> snapshot   |  |        |
| $\alpha = 0^\circ$<br>Simple shear | $\epsilon_{bg} = 17.3\%$   | $\epsilon_{bg} = 30.6\%$   | $\epsilon_{bg} = 41.5\%$   |  |        |
|                                    | $ \vec{\lambda}_{min}  = 0.91$<br>$ \vec{\lambda}_{max}  = 1.10$ | $ \vec{\lambda}_{min}  = 0.84$<br>$ \vec{\lambda}_{max}  = 1.20$ | $ \vec{\lambda}_{min}  = 0.77$<br>$ \vec{\lambda}_{max}  = 1.30$ |  |        |
| $\alpha = 30^\circ$                | $\epsilon_{bg} = 7.7\%$  | $\epsilon_{bg} = 14.4\%$   | $\epsilon_{bg} = 20.2\%$   |  |        |
|                                    | $ \vec{\lambda}_{min}  = 0.95$<br>$ \vec{\lambda}_{max}  = 1.02$ | $ \vec{\lambda}_{min}  = 0.89$<br>$ \vec{\lambda}_{max}  = 1.04$ | $ \vec{\lambda}_{min}  = 0.85$<br>$ \vec{\lambda}_{max}  = 1.06$ |  |        |
| $\alpha = 45^\circ$                | $\epsilon_{bg} = 6.3\%$  | $\epsilon_{bg} = 11.8\%$   | $\epsilon_{bg} = 16.9\%$   | $\epsilon_{bg} = 17.3\%$   |        |
|                                    | $ \vec{\lambda}_{min}  = 0.95$<br>$ \vec{\lambda}_{max}  = 1.01$ | $ \vec{\lambda}_{min}  = 0.90$<br>$ \vec{\lambda}_{max}  = 1.02$ | $ \vec{\lambda}_{min}  = 0.86$<br>$ \vec{\lambda}_{max}  = 1.03$ | $ \vec{\lambda}_{min}  = 0.85$<br>$ \vec{\lambda}_{max}  = 1.03$ |        |
| $\alpha = 60^\circ$                | $\epsilon_{bg} = 5.8\%$  | $\epsilon_{bg} = 10.4\%$   | $\epsilon_{bg} = 15.2\%$   |  |        |
|                                    | $ \vec{\lambda}_{min}  = 0.95$<br>$ \vec{\lambda}_{max}  = 1.00$ | $ \vec{\lambda}_{min}  = 0.91$<br>$ \vec{\lambda}_{max}  = 1.01$ | $ \vec{\lambda}_{min}  = 0.86$<br>$ \vec{\lambda}_{max}  = 1.01$ |  |        |
| $\alpha = 90^\circ$<br>Pure shear  | $\epsilon_{bg} = 5.4\%$  | $\epsilon_{bg} = 10.0\%$   | $\epsilon_{bg} = 14.0\%$   |  |        |
|                                    | $ \vec{\lambda}_{min}  = 0.95$<br>$ \vec{\lambda}_{max}  = 1.00$ | $ \vec{\lambda}_{min}  = 0.91$<br>$ \vec{\lambda}_{max}  = 1.00$ | $ \vec{\lambda}_{min}  = 0.87$<br>$ \vec{\lambda}_{max}  = 1.00$ |  |        |

### 2.3. Calculation of 3D fold amplitudes and fold axis orientation

From the FE-simulations, all three fold amplitudes are calculated based on the z-coordinates of the folded upper interface of the top layer (i.e., the model topography). Fig. 2 depicts the definitions of the three fold amplitudes.

- The amplitude in z-direction (vertical),  $A_z$ , is defined as the maximum z-coordinate value above the mean model topography. Because the model and the initial perturbation are centered at ( $x = 0, y = 0$ ), the amplitude in z-direction corresponds to the topography at the model center.
- The amplitude parallel to the fold axis,  $A_{\parallel}$ , corresponds to the distance between the model center (i.e., locus of initial perturbation) and the furthest point on the topographic contour line of the 0<sup>th</sup> sequential fold (i.e., initial fold) at an absolute value of  $A_0/2$  measured along the fold axis.
- The amplitude perpendicular to the axial plane,  $A_{\perp}$ , corresponds to the distance between the model center (i.e., locus of initial perturbation) and the furthest point on a topographic contour line at an absolute value of  $A_0/2$  measured along the normal vector to the axial plane.

The initial values for the three amplitudes based on the initial perturbation,  $G$  (Eq. (3)), are  $A_{z,ini} = A_0$  and  $A_{\parallel,ini} = A_{\perp,ini} = \lambda_0/4$ . These initial values are used for normalizing the amplitude values in the respective directions.

Equivalent to the bulk fold structure, amplitudes of the individual sequential folds (i.e., individual anti- and synforms) are calculated. For the  $i^{\text{th}}$  sequential fold, these amplitudes are labeled  $A_{z,i}$ ,  $A_{\parallel,i}$ , and  $A_{\perp,i}$ . Consequently, the following equalities apply:  $A_z = A_{z,0}$  and  $A_{\parallel} = A_{\parallel,0}$ ; in words, the amplitudes in z-direction and parallel to the fold axis are respectively the same for the bulk fold structure and for the 0<sup>th</sup> sequential fold (i.e., initial fold).

In addition, the orientation of the fold axis (i.e., angle relative to x-axis) of both the bulk fold structure and of each individual sequential

fold is calculated by fitting an ellipse to each topographic  $A_0/2$ -contour line and determining the orientation of its major axis.

### 2.4. Calculation of fold growth rates

In the infinitesimal-amplitude stage, folds grow exponentially with time (e.g., Biot, 1961; Fletcher, 1991, 1977; Schmalholz, 2006). To quantify the fold growth rates, this assumption is also used for the finite-amplitude stages modeled in this study. However, in the present cases, this assumption only makes sense in the vertical direction and parallel to the fold axis (see results below); hence the following amplitude evolution laws are assumed:

$$A_z = A_{z,ini} \exp[(q_z + q_{z,k}) \dot{\epsilon}_{bg} t] \Leftrightarrow A_z = A_{z,ini} (1 - \epsilon_{bg})^{-(q_z + q_{z,k})}, \quad (6)$$

$$A_{\parallel} = A_{\parallel,ini} \exp[(q_{\parallel} + q_{\parallel,k}) \dot{\epsilon}_{bg} t] \Leftrightarrow A_{\parallel} = A_{\parallel,ini} (1 - \epsilon_{bg})^{-(q_{\parallel} + q_{\parallel,k})}, \quad (7)$$

where  $(q_z + q_{z,k})$  and  $(q_{\parallel} + q_{\parallel,k})$  are the total growth rates in the vertical direction and parallel to the fold axis, respectively. These growth rates consist of an active part (due to the mechanical buckling instability) and a passive (kinematical; denoted with subscript  $k$ ) part due to the background strain field. In the vertical direction, the kinematical amplification rate reflects the pure-shear component of the applied boundary conditions given as

$$q_{z,k} = \sin(\alpha). \quad (8)$$

Parallel to the fold axis, the kinematical elongation rate can be determined from the elongating major horizontal principal strain axis, which results in

$$q_{\parallel,k} = \sin^2(45 - \alpha/2). \quad (9)$$

The active fold growth rates,  $q_z$  and  $q_{\parallel}$ , can then be obtained by fitting Eqs. (6) and (7) to the corresponding amplitude evolution data.

## 3. Results

Fig. 3 shows a selection of simulation snapshots in top view. For all convergence angles, the fold structure grows in all three directions with increasing background strain. Fold amplification (vertical) leads to increasing topography (indicated by color in Fig. 3), fold elongation yields elongation of the topographic  $A_0/2$ -contour lines parallel to the fold axis, and sequential folds growth gives rise to new sequentially appearing topographic contour lines.

Already from these simulation snapshots it is evident that the fold growth rates in all three directions, as well as the ratios between the three directions, depend on the convergence angle. For example, the background strain necessary for the 3<sup>rd</sup> sequential fold to appear (right snapshots in Fig. 3) is larger for smaller convergence angles; hence sequential fold growth is slower for smaller convergence angles. At the same time, the fold amplitude (vertical) at the moment the 3<sup>rd</sup> sequential fold appears is smaller for smaller convergence angles, while the elongation of the initial fold (0<sup>th</sup> sequential fold) is larger; hence the ratio between fold amplification and fold elongation decreases with decreasing convergence angle. The 3D fold growth is investigated in further detail in the first sub-section below.

Also evident from the simulation snapshots (Fig. 3) is that the orientation of the fold axis in top view is a function of the convergence angle. The angle of the fold axis with respect to the x-axis is zero for pure shear and increases with decreasing convergence angle. This is investigated in further detail in the second sub-section below.

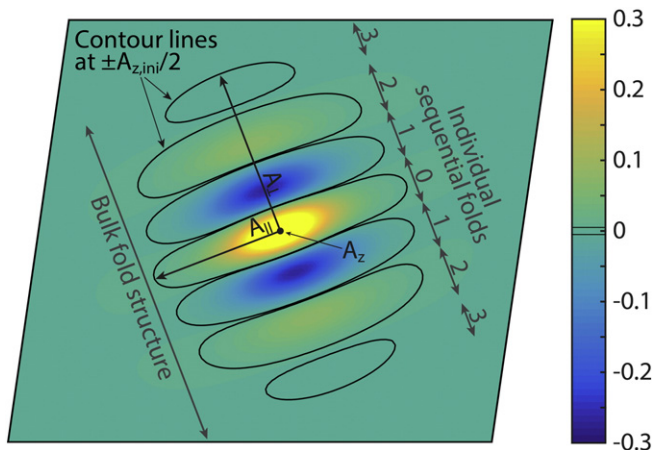


**Fig. 2.** Example simulation snapshot in top view (x-axis to the right) to illustrate the definitions of the three fold amplitudes. The selected snapshot corresponds to a model with  $R = 100$  and  $\alpha = 45^\circ$  after 17.3% background strain. Colors represent the model topography above a reference level (i.e., zero mean topography); thin black contour lines mark half the initial value ( $A_0/2$ ). Fold amplitude  $A_z$  (vertical) corresponds to the maximum elevation (indicated as a dot); fold amplitudes  $A_{\parallel}$  (parallel to fold axis) and  $A_{\perp}$  (perpendicular to axial plane) are defined by the lateral extent of the black contour lines. In addition, the difference between the bulk fold structure and the individual sequential folds (individual syn- and antiforms) and their consecutive numbering is indicated.

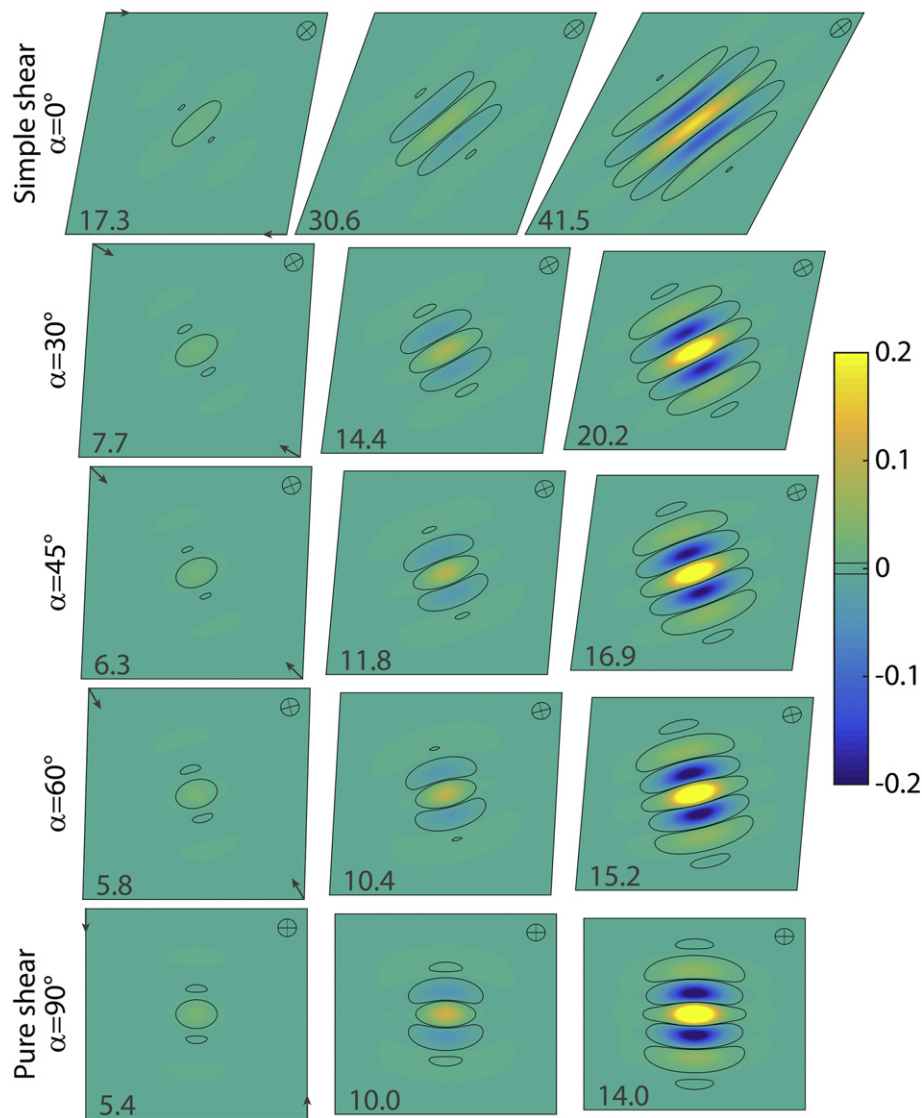


**Fig. 3.** Snapshots of selected numerical simulations ( $R = 100$ ) in top view ( $x$ -axis to the right). Snapshots from top to bottom correspond to different convergence angles given on the left and indicated with gray arrows. Background strain,  $\epsilon_{bg}$ , is increasing from left to right for each convergence angle and is given in each snapshot in %. Colors represent the vertical fold amplitude ( $z$ -direction); thin black contour lines mark half the initial value ( $A_0/2$ ), which defines the individual sequential folds. The snapshots are chosen always immediately after the first appearance of new sequential folds. The upper-right corner of each snapshot shows the horizontal strain ellipse with its major and minor axes. Consult Table 1 to translate background strain ( $\epsilon_{bg}$ ) to the lengths of the minor ( $|\vec{\lambda}_{min}|$ ) and major ( $|\vec{\lambda}_{max}|$ ) horizontal principal strain axes.

### 3.1. 3D fold growth and lateral fold aspect ratio

Figs. 4 and 5 show the normalized fold amplitude evolution in all three directions and the lateral fold aspect ratio (i.e.,  $A_{||}/A_{\perp}$ -ratio) for the same five simulations as shown in Fig. 3 ( $R = 100$ ). At the beginning of each simulation, all normalized fold amplitudes and the lateral fold aspect ratio are equal to 1 representing the initial condition (Eq. (3)). After that, the general fold growth is very similar for all convergence angles, yet at different rates.

The initial isolated fold ( $0^{\text{th}}$  sequential fold) grows in both the vertical direction (increasing  $A_{z,0}$ ; thin solid line in Fig. 4) and parallel to the fold axis (increasing  $A_{||,0}$ ; thin dashed line). At the same time, the extent perpendicular to the axial plane ( $A_{\perp,0}$ ; thin dotted line) is restricted to the dominant wavelength,  $\lambda_0$  (Eq. (4)), and is actually slightly decreasing with increasing background strain ( $A_{\perp,0}/\lambda_0 < 1$  in Fig. 4), representing tightening of the fold. This demonstrates that perpendicular to the axial plane, the bulk fold structure does not grow as a single individual fold but grows due to the appearance of new sequential folds adjacent to the initial one.

When new sequential folds appear, they are already elongated (thin lines in Fig. 5) and continue elongating (parallel to fold axis) and growing in the vertical direction; but again, their extent perpendicular to the axial plane is restricted to the dominant wavelength (Fig. 4).

For the bulk fold structure, the amplitudes in the vertical direction ( $A_z$ ) and parallel to the fold axis ( $A_{||}$ ) are the same as for the initial isolated fold ( $0^{\text{th}}$  sequential fold). Growth perpendicular to the axial plane ( $A_{\perp}$ ; bold dotted line in Fig. 4) is marked by jumps every time a new sequential fold appears and therefore the bulk fold structure suddenly occupies more space (see also Fig. 3). Despite these jumps, the average sequential fold amplitude (perpendicular to the axial plane) is similar to the elongation of the fold (parallel to the fold axis). Therefore, the lateral fold aspect ratio of the bulk fold structure oscillates around a value of 1 (bold line in Fig. 5); for small convergence angles, the bulk lateral fold aspect ratio tends to be slightly above 1; for larger convergence angles, the bulk lateral fold aspect ratio tends to be slightly below 1.

To quantify the initial fold growth rates, Eqs. (6) and (7) are fit to the amplitude-vs.-time data of the  $0^{\text{th}}$  sequential fold equivalent to the first

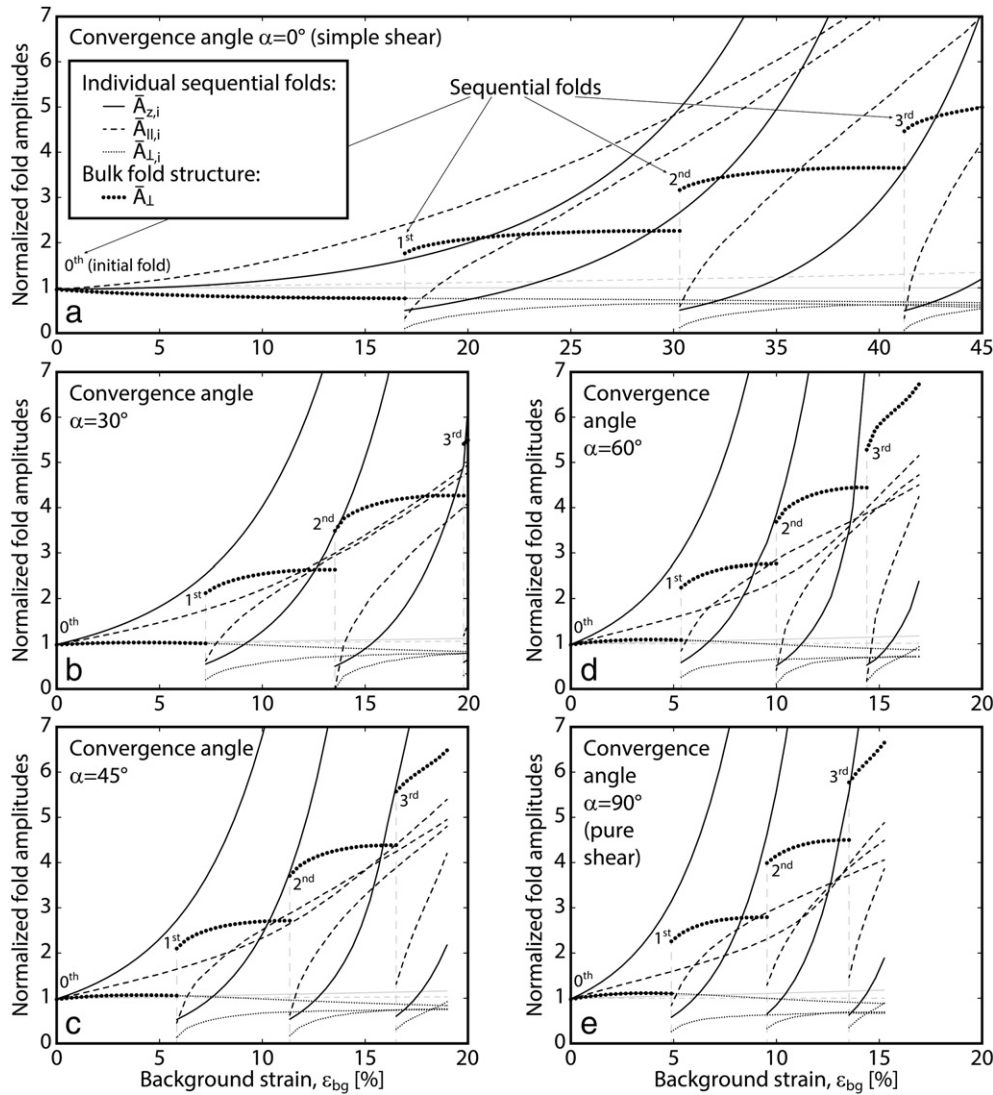


**Fig. 4.** Fold amplitude evolution in all three directions of both the individual sequential folds (individual anti- and synforms; thin lines) and the bulk fold structure (bold dotted lines) for the same simulations shown in Fig. 3 ( $R = 100$ ) with increasing background strain,  $\epsilon_{bg}$ , and for different convergence angles (subfigures a–e). Parallel to the fold axis ( $A_{||}$ ) and in vertical direction ( $A_z$ ), amplitudes of the bulk fold structure are equal to the respective amplitudes of the initial fold ( $0^{th}$  sequential fold). All amplitudes are normalized by their respective initial value ( $\bar{A}_z = A_z/A_{z,ini}$ ,  $\bar{A}_{||} = A_{||}/A_{||,ini}$ ,  $\bar{A}_{\perp} = A_{\perp}/A_{\perp,ini}$ ). Vertical gray dashed lines mark the first appearances of new sequential folds (i.e., snapshots in Fig. 3); sub-horizontal gray lines show the kinematical growth in z-direction (solid gray lines) and parallel to the fold axis (dashed gray line). Note that all subfigures have the same vertical and horizontal scale and the legend in a) is valid for all subfigures.

10% of background strain shown in Fig. 4 ( $R = 100$ ), as well as to the equivalent data for other convergence angles not shown in Fig. 4 and for a viscosity ratio of  $R = 20$ . The obtained initial fold growth rates in the vertical direction and parallel to the fold axis are plotted in Fig. 6 as a function of convergence angle. Fold growth rates are significantly lower for the lower viscosity ratio, as expected from theory (Fletcher, 1991). However, the general trend with convergence angle is independent of viscosity ratio. Both growth rates increase with increasing convergence angle, indicating that folds grow faster in pure shear than in simple shear (also discernible in Fig. 3). In the vertical direction, this dependency on convergence angle is stronger than it is parallel to the fold axis; hence the ratio of fold amplification (vertical) to fold elongation (parallel to fold axis) also increases with increasing convergence angle. For convergence angles larger than about  $15^\circ$ , fold amplification exhibits a higher rate than fold elongation (Fig. 6). Only for cases close to simple shear is fold elongation faster than fold amplification. The rate of sequential fold growth is not quantified here because it exhibits abrupt jumps and it is therefore not straightforward to fit Eqs. (6) and (7) to the amplitude evolution data. However, Fig. 4 suggests that

the average rate of sequential fold growth is close to the rate of fold elongation.

### 3.2. Fold axis orientation

Fig. 7 shows the evolution of the fold axis orientation in top view (angle relative to x-axis) as a function of background strain and convergence angle and for two viscosity ratios,  $R = 100$  (Fig. 7a) and  $R = 20$  (Fig. 7b). The initial perturbation is circular (Eq. (3)) and no fold orientation can be determined. As soon as the fold starts growing, the fold axis elongates in the direction of the major horizontal instantaneous stretching axis ( $\vec{ISA}_{max}$ , given as  $45^\circ - \alpha/2$ ). This particular orientation of folds at their initiation has been suggested by previous analytical and modeling studies (Fossen et al., 2013; James and Watkinson, 1994; Tikoff and Peterson, 1998; Treagus and Treagus, 1981). With increasing background strain, the fold axis rotates and stays parallel to the major horizontal principal strain axis ( $\vec{\lambda}_{max}$ , i.e., long axis of the horizontal strain ellipse).

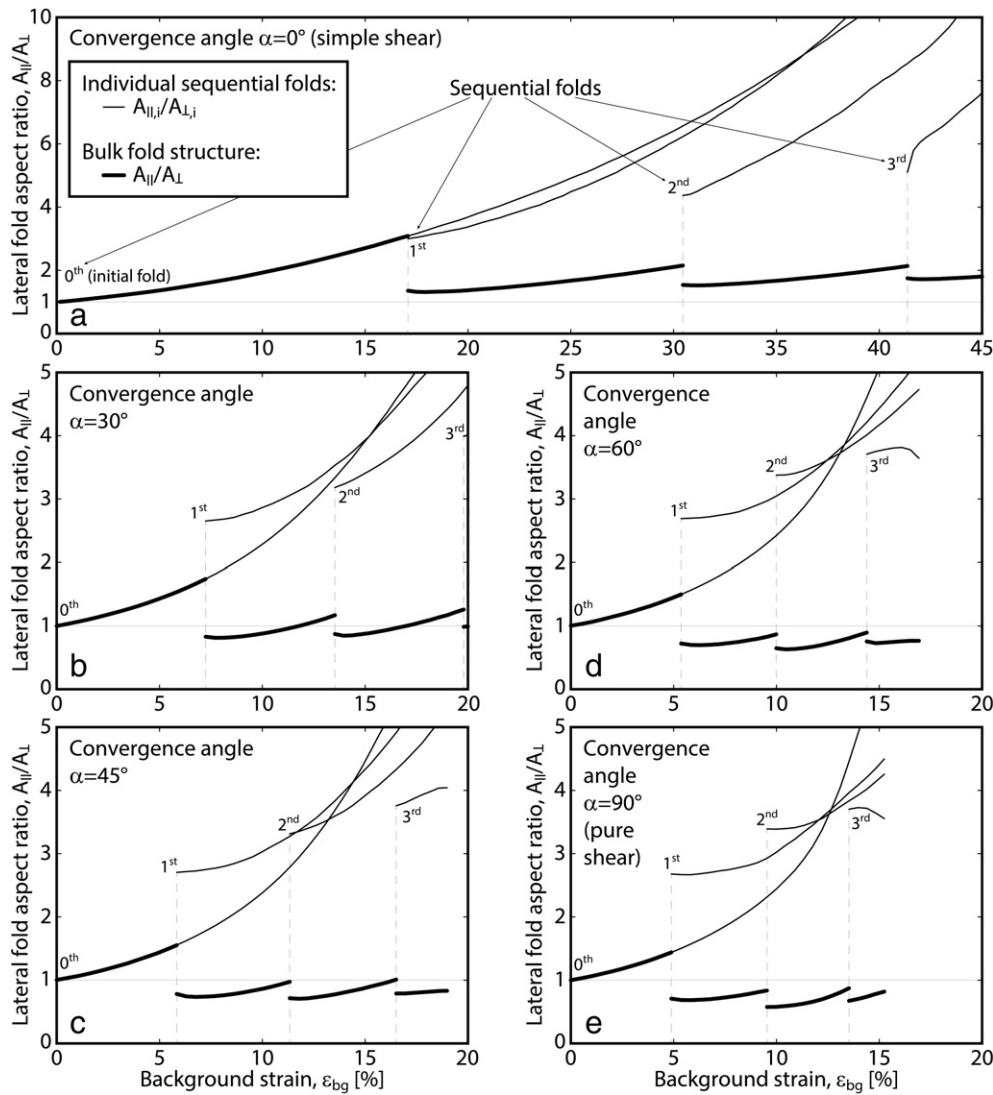


**Fig. 5.** Evolution of the lateral fold aspect ratio (in top view; i.e.,  $A_{||}/A_{\perp}$ -ratio) of both the individual sequential folds (individual anti- and synforms; thin lines) and the bulk fold structure (bold lines) for the same simulations shown in Fig. 3 ( $R = 100$ ) with increasing background strain,  $\epsilon_{bg}$ , and for different convergence angles (subfigures a–e). Vertical gray lines mark the first appearances of new sequential folds (i.e., snapshots in Fig. 3); horizontal gray lines indicate the initial lateral fold aspect ratio (i.e., 1). Note that all subfigures have the same vertical and horizontal scale, except subfigure a), which is vertically compressed by a factor of 2; the legend in a) is valid for all subfigures. This figure directly derives from the data shown Fig. 4.

When new sequential folds appear, their fold axes do not initiate parallel to  $\vec{ISA}_{max}$ , but rather parallel to  $\vec{\lambda}_{max}$ . In other words, sequential folds initiate parallel to the already existing folds and continue rotating together with them.

Because in the initial state, the major horizontal principal strain axis is parallel to the major horizontal instantaneous stretching axis ( $\vec{\lambda}_{max,ini} = \vec{ISA}_{max}$ ), the general statement can be made that in the presented cases, fold axes are always oriented parallel to the major horizontal principal strain axis,  $\vec{\lambda}_{max}$ . They initiate in this orientation and then rotate together with  $\vec{\lambda}_{max}$ . Importantly, this statement is independent of convergence angle and viscosity ratio. Viscosity ratio only affects the rate at which folds grow but not their orientation.

### 3.3. Hinge migration

As the orientation of  $\vec{\lambda}_{max}$  is not a material line, the fold axis being parallel to  $\vec{\lambda}_{max}$  implies hinge migration during fold growth. In other words, fold hinges are not fixed to the material, but material migrates

through the fold hinge from one limb to the other. To visualize this, Fig. 8 shows oblique views of the highest-strain snapshots for each convergence angle shown in Fig. 3 together with the orientation of  $\vec{\lambda}_{max}$  (red line) and a passive material line initially parallel to  $\vec{ISA}_{max}$  (black line). In all snapshots, the view direction is along  $\vec{ISA}_{max}$  (or  $\vec{\lambda}_{max,ini}$ ); hence the misalignment of the black and red line with respect to the view direction represents the passive rotation of the material line and the rotation of  $\vec{\lambda}_{max}$ , respectively.

From (Figs. 7 and 8) it is evident that during the early stages of folding, the fold axis exhibits a lower rotation rate than the passive material line. As a consequence, material between the red and black lines in Fig. 8 has migrated through the fold hinge; material immediately on the opposite side of the red line compared to the black line will migrate through the fold hinge with further background strain. In other words, the fold hinge migrates through the material and is not a fixed material line. This hinge migration is more marked for smaller convergence angles and disappears completely for pure shear, where  $\vec{\lambda}_{max}$  is parallel to  $\vec{ISA}_{max}$  throughout the simulation.

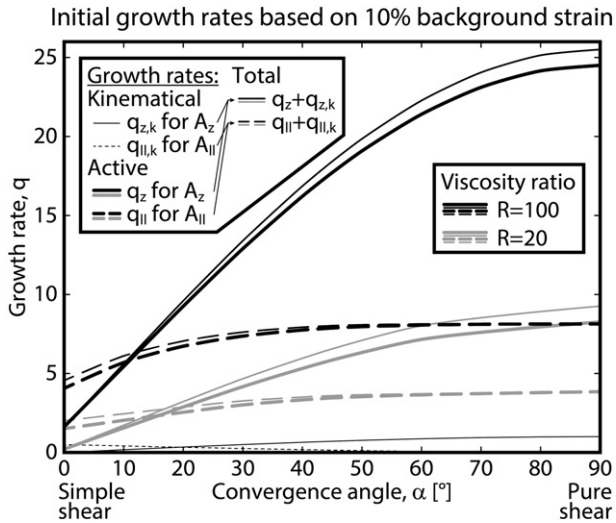


**Fig. 6.** Active growth rate in vertical direction ( $q_z$ , bold solid lines) and parallel to the fold axis ( $q_k$ , bold dashed lines) of the 0<sup>th</sup> sequential fold (initial fold) during the earliest folding stage as a function of convergence angle and for two viscosity ratios,  $R = 100$  (black lines) and  $R = 20$  (gray lines). Also shown are the kinematical growth rates in both directions,  $q_{z,k}$  and  $q_{k,k}$ , as well as the sum of the kinematical and the active growth rates. To calculate the total growth rates, an exponential curve is fit to the respective amplitude-vs.-time data equivalent to the first 10% of background strain in Fig. 4 (for  $R = 100$ ) and to the equivalent data (not shown here) for  $R = 20$ .

**4. Discussion**

Simplified test cases have been presented to investigate first-order phenomena of 3D folding in transpression. The simplifications lie in the linear viscous (Newtonian) rheology, the two-layer model setup, the relatively small applied background strain, and the absence of surface processes and gravity. From 2D analytical studies it is known that incorporating gravity decreases the fold amplification rate (vertical) (Schmalholz et al., 2002). Surface processes (erosion of antiforms, deposition in synforms) increase the fold amplification rate (Collignon et al., 2014; Simpson, 2004). In addition, Collignon et al. (2014) used a fully 3D coupled mechanical-surface processes numerical model to show that surface processes do not significantly alter the lateral

fold aspect ratio and the general fold pattern in pure shear ( $\alpha = 90^\circ$ ). Yamato et al. (2011) used a 2D visco-elasto-plastic multilayer model to simulate folding in the Zagros fold-and-thrust-belt. They obtained periodic folding with similar amplification rate curves as for Newtonian single-layer models. These results suggest that more complicated rheologies, multilayer settings, and surface processes may alter fold growth rates, but not the fundamental folding mechanisms. Therefore, the key observations in this study, such as the fold axis rotation with  $\vec{\lambda}_{max}$  or the almost constant lateral fold aspect ratio of 1, are expected to still hold for natural fold structures.

**4.1. Active versus passive 3D fold growth**

In the vertical direction, kinematical extension due to the background strain field contributes to the amplification of the fold. Therefore, the total amplification rate,  $q_z + q_{z,k}$ , presented in Fig. 6 (thin solid lines) incorporates both the active amplification (due to the mechanical buckling instability,  $q_z$ ) and the passive (kinematical,  $q_{z,k}$ ) amplification. The latter is maximal for pure shear, where it is equal to 1 (e.g., Biot, 1961), and zero for simple shear (Eq. (8)), for which no kinematical vertical extension occurs. In any case, the active amplification significantly outpaces the kinematical one (Fig. 6).

Similarly, kinematical extension due to the background strain field also contributes to fold elongation (parallel to fold axis). The kinematical contribution corresponds to the elongation of the horizontal strain ellipse, which is displayed in Fig. 3 and whose long axis,  $|\vec{\lambda}_{max}|$ , is listed in Table 1. The corresponding kinematical elongation rate,  $q_{k,k}$  (Fig. 6), is maximal for simple shear, where it is equal to 0.5 (Eq. (9)), and zero for pure shear, for which the horizontal strain ellipse is not extended. In any case, the active fold elongation significantly outpaces the kinematical one. This is confirmed by comparing the strain ellipses and the lateral fold aspect ratio in Fig. 3 for a viscosity ratio of  $R = 100$ , where the latter outpaces the former. Perpendicular to the axial plane, the direction of sequential fold growth coincides with the orientation of the minor horizontal principal strain axis,  $\vec{\lambda}_{min}$  (Fig. 3). In other words, sequential fold growth has to work against the background strain field. All in all, this demonstrates that fold growth in the two lateral directions is predominantly an active process due to the mechanical buckling instability.

Even though the 3D growth of a fold structure is caused by one single background strain field, the mode of growth in all three directions

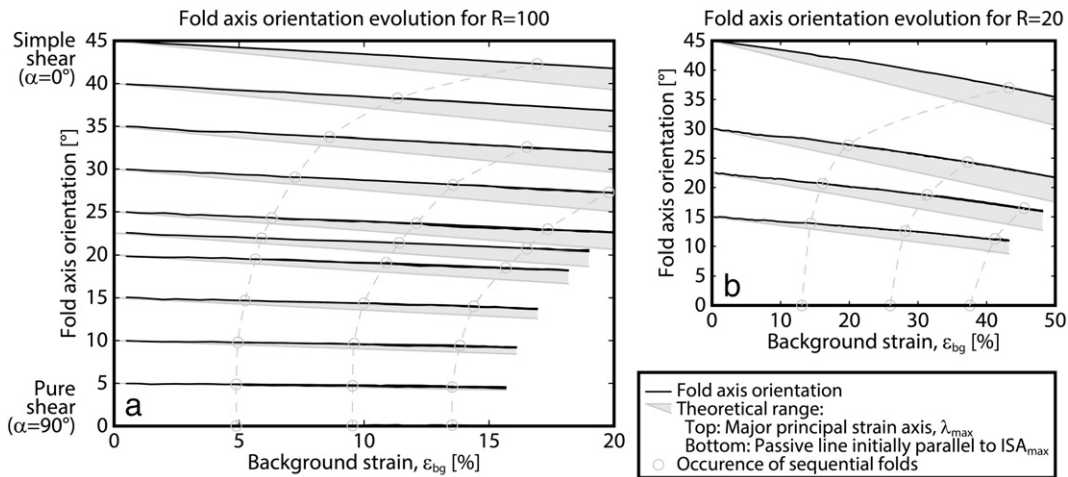


**Fig. 7.** Evolution of fold axis orientation in top view (angle with respect to x-axis) of all individual sequential folds (individual anti- and synforms; black lines) with increasing background strain,  $\epsilon_{bg}$ , for different convergence angles (from  $\alpha = 0^\circ$ , simple shear to  $\alpha = 90^\circ$ , pure shear) and for two different viscosity ratios,  $R = 100$  (a) and  $R = 20$  (b). Note that subsequent sequential folds have virtually the same orientation as the preceding ones; hence the data are hardly distinguishable even though the data for all sequential folds are plotted. Gray areas outline the theoretical range of fold axis orientation for each convergence angle after (Fossen et al., 2013); top edges indicate the orientation of the major horizontal principal strain axis ( $\vec{\lambda}_{max}$ ); bottom edges indicate the orientation of a passive material line initially parallel to the major horizontal instantaneous stretching axis ( $ISA_{max}$ ). In b) more background strain is shown because folds grow at a lower rate.

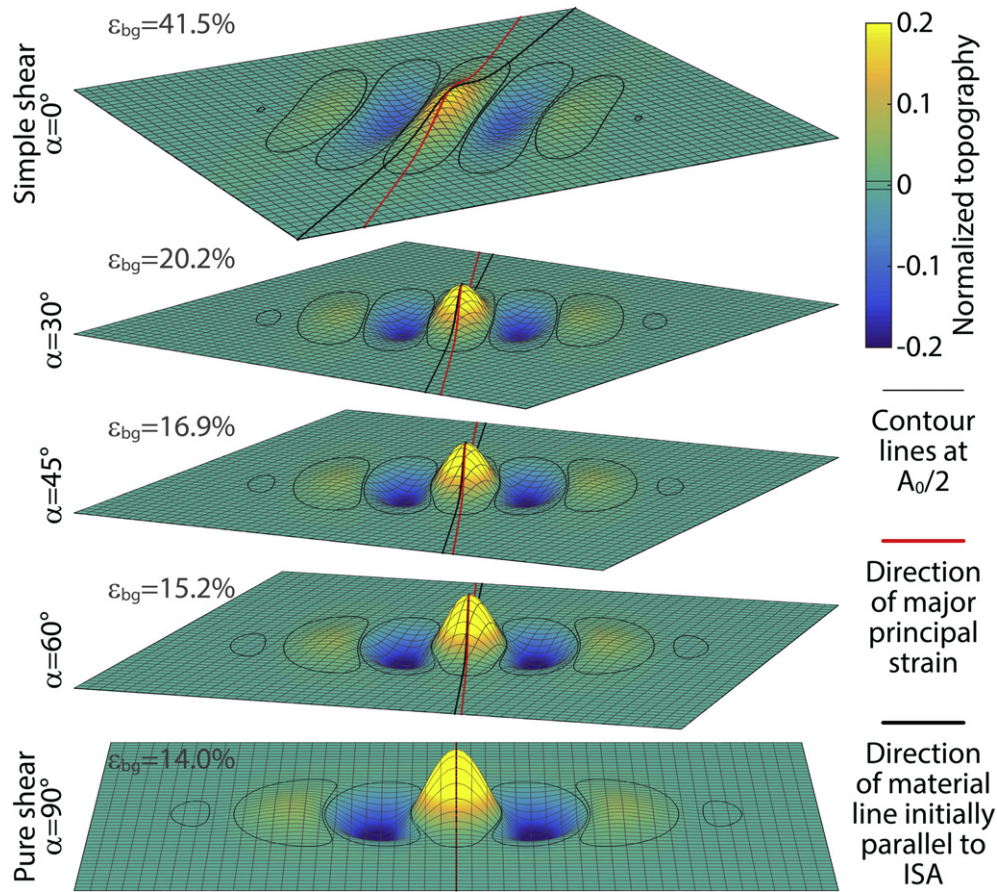


**Fig. 8.** Oblique view (20 times vertically exaggerated) of the snapshots shown in Fig. 3 ( $R = 100$ ) at the respective largest background strain (indicated in each panel) of each convergence angle (indicated on the left). The view direction is always along the major horizontal instantaneous stretching axis ( $\vec{ISA}_{\max}$ ). The bold black line indicates the orientation of a material line that was initially parallel to the view direction and has passively rotated away from this orientation; the bold red line indicates the orientation of the major horizontal principal strain axis ( $\vec{\lambda}_{\max}$ ; i.e., fold axis).

is quite different. In the two lateral directions, the growing fold structure incorporates more and more material further and further away from the initiation point while growth in the vertical direction (fold amplification) does not incorporate additional material with increasing deformation.

#### 4.2. Rotation of fold axis and comparison with Leever et al. (2011)

The initial fold in transpression has a fold axis parallel to  $\vec{ISA}_{\max}$  (or  $\vec{\lambda}_{\max, \text{ini}}$ ; Fig. 7). It has been debated how this fold axis rotates with increasing deformation. Grujic and Mancktelow (1995) and model 1 of Fossen et al. (2013) suggested that the fold axis is fixed to a material line and rotates passively; Tikoff and Peterson (1998) and model 2 of Fossen et al. (2013) suggested that the fold axis rotates actively and stays parallel to  $\vec{\lambda}_{\max}$ . The presented results indicate that the latter model is correct, which also implies hinge migration during progressive deformation in transpression. Grujic and Mancktelow (1995) used non-linear viscous analog materials (paraffin wax) with an effective viscosity ratio of  $R \approx 600$  and a power-law stress exponent of 2.4–2.7. However, the difference in material properties compared to the presented study is not sufficient to explain the fundamental difference in results. The reason why in the analog models of Grujic and Mancktelow (1995) the fold axis was fixed to the material and did not migrate (N.S. Mancktelow, personal communication) may be that the employed paraffin wax did not exhibit pure viscous rheology, but also behaved

slightly brittlely. When the fold amplifies during the early experimental stages, micro-cracks may develop where the curvature is largest, which is along the initial fold axis parallel to  $\vec{ISA}_{\max}$ . Therefore, the material is strongly weakened along  $\vec{ISA}_{\max}$ , which prohibits the migration of the fold axis with increasing deformation and the fold rotates passively as a material line.

Whether these observations are also applicable to transtension remains to be studied in the future. However, the analog experiments of Venkat-Ramani and Tikoff (2002) suggest that also in transtension the fold axis initializes parallel to  $\vec{ISA}_{\max}$  and then rotates and stays parallel to  $\vec{\lambda}_{\max}$ ; hence model 2 of Fossen et al. (2013) would also be the correct choice in transtension.

To test if also in a real-world situation the fold axis initiates parallel to  $\vec{\lambda}_{\max}$  and then rotates actively to stay parallel to this orientation, the data of Leever et al. (2011) is used. They present data of the progressive rotation of a fold hinge with increasing deformation in a transpressional analog model with a convergence angle of  $\alpha = 15^\circ$ . Fig. 9 shows this data together with the theoretical curves for the orientation of  $\vec{\lambda}_{\max}$  (i.e., the theoretical fold axis orientation) and of a passive line initially parallel to  $\vec{ISA}_{\max}$ . Leever et al. (2011) measure the displacement applied at the boundaries of their model in absolute units (cm) and not in dimensionless units, such as  $\epsilon_{\text{bg}}$ . Therefore,  $\epsilon_{\text{bg}}$  is translated to these absolute units using either side length of their modeling box as the reference length (Fig. 3 in Leever et al., 2011); hence two slightly

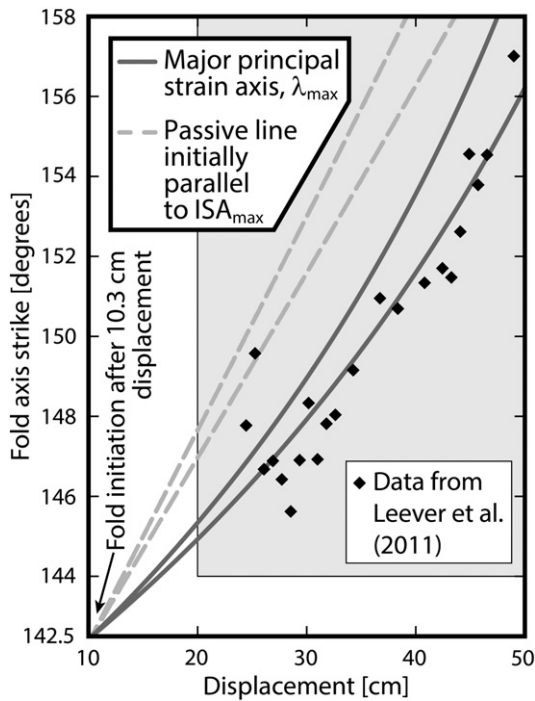


**Fig. 9.** Data of Leever et al. (2011) of the progressively rotating fold axis in a transpressional analog experiment (black diamonds) together with theoretical fold axis orientations,  $\vec{\lambda}_{\max}$  (dark gray lines) and passive line initially parallel to  $\vec{ISA}_{\max}$  (dashed light gray lines). Both axes have the same units as in Leever et al. (2011). Because they use absolute units (cm) for the externally applied displacement, the non-dimensional background strain,  $\varepsilon_{bg}$ , is translated to these absolute units using either of the two side lengths of the modeling box of Leever et al. (2011) as the reference length (60 cm, lower lines or 52 cm, upper lines). Leever et al. (2011) state that folding initiates after 10.3 cm external displacement; hence the theoretical curves are plotted from this initiation point. A fold axis orientation of 142.5° corresponds to the orientation of  $\vec{ISA}_{\max}$ .

different theoretical curves are obtained. In Leever et al. (2011), folding initiates only after an initial phase of distributed strain, which accommodates 10.3 cm of externally applied displacement. Therefore, the theoretical curves are only plotted after fold initiation. The theoretical fold orientation curves ( $\vec{\lambda}_{\max}$ ) almost perfectly match the analog modeling data (Fig. 9) while the orientation of the passive line does not fit the data well. This confirms that folds initiate and stay parallel to  $\vec{\lambda}_{\max}$ . Interestingly, Leever et al. (2011) only plot the fold orientation after quite substantial external displacement (long after initiation; supposedly only after they could identify the fold safely). Consequently, the fold axis orientation at their lowest-displacement data point is not parallel to  $\vec{ISA}_{\max}$  (142.5°), but the fold axis has already rotated unnoticed together with  $\vec{\lambda}_{\max}$ .

#### 4.3. Application to the NW Zagros Simply Folded Belt

For natural folds, it is hardly possible to track the fold axis orientation over geological time scales. However, the presented study together with the excellent fit of the data of Leever et al. (2011) gives confidence that also natural fold axes are oriented parallel to  $\vec{\lambda}_{\max}$ . Hence there is a triangular relationship between convergence angle,  $\alpha$ , amount of background strain,  $\varepsilon_{bg}$  (or any other strain measure), and fold axis orientation. Theoretically, if two of these values are known, the third can be determined.

To illustrate this, fold axis orientation data of the north-westernmost Zagros Mountains (NE Iraq) are considered in Fig. 10. In this area, the Zagros Simply Folded Belt (ZSFB) is bounded in the North-East by the

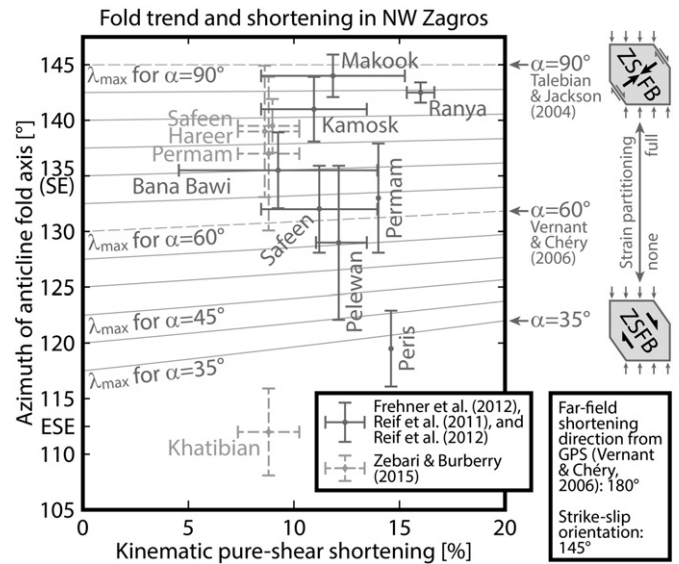


**Fig. 10.** Fold axis orientations plotted versus kinematic strain estimates of anticlines in the NW Zagros Simply Folded Belt (ZSFB; NE Iraq). Orientation data are taken directly from Reif et al. (2011), Reif et al. (2012), and Zebari and Burberry (2015) or are estimated from maps provided in these three publications; shortening estimates are taken directly from Frehner et al. (2012) and Reif et al. (2011) or are calculated based on the cross-section provided in Zebari and Burberry (2015). In the background, the theoretical fold axis orientation,  $\vec{\lambda}_{\max}$ , is plotted for different convergence angles. End-member convergence angles are sketched on the right based on the far-field shortening direction and strike-slip fault orientation; they are 90° (pure shear) for full strain partitioning and 35° for zero strain partitioning.

Main Zagros Thrust (MZT) and the Main Recent Fault (MRF) striking about 145° (Zebari and Burberry, 2015; Reif et al., 2012, 2011). The far-field shortening direction has been inferred from GPS measurements as almost perfectly north-south (i.e., 180°; Vernant and Chéry, 2006) leading to a far-field convergence angle of  $\alpha = 35^\circ$ . The shortening is partitioned between the ZSFB and the MZT-MRF-fault system, whereas the latter exhibits a right-lateral strike-slip component. However, there has been some dispute about the amount of strain partitioning in the Zagros Mountains. Based on earthquake focal mechanisms, Talebian and Jackson (2004) proposed full partitioning implying that 100% of the far-field strike-slip component is accommodated by the MZT-MRF-fault system and the ZSFB experiences pure shortening with a convergence angle of  $\alpha = 90^\circ$  (upper sketch in Fig. 10). The other end-member case – zero strain partitioning – implies that the MZT-MRF-fault system does not accommodate any strike-slip movement and the ZSFB experiences oblique convergence with a convergence angle equal to the far-field one (i.e.,  $\alpha = 35^\circ$ ; lower sketch in Fig. 10). However, this model is unrealistic because some strike-slip movement along the MZT-MRF-fault system has clearly been documented (Talebian and Jackson, 2002). Based on Masson et al. (2005), Vernant and Chéry (2006) proposed an intermediate strain partitioning model, in which only a part of the far-field strike-slip component is accommodated by the MZT-MRF-fault system, leaving the ZSFB with a convergence angle of  $\alpha = 60^\circ$ .

Fig. 10 shows the fold axis orientation of various anticlines of the ZSFB in NE Iraq plotted versus the kinematical shortening estimates. The latter are determined from restored geological cross-sections perpendicular to the fold axis orientation (Zebari and Burberry, 2015; Frehner et al., 2012; Reif et al., 2012, 2011); hence they correspond to pure-shear shortening,  $\varepsilon_{ps}$  (Appendix C), and not to background strain,  $\varepsilon_{bg}$ , as for example in Fig. 7. Fig. 10 also shows the theoretical fold axis orientation,  $\vec{\lambda}_{\max}$ , for different convergence angles. Despite some data scatter, the orientation of the majority of fold axes indicates a convergence angle within the ZSFB of  $\alpha = 60^\circ$ – $90^\circ$  confirming the proposed

range of Vernant and Chéry (2006) ( $\alpha = 60^\circ$ ) and Talebian and Jackson (2004) ( $\alpha = 90^\circ$ ). However, the data covers this entire range of convergence angles; hence it is not clear which end-member model is more appropriate.

There are two main factors influencing the presented data. First, the observed folds in the ZSFB may not be individual structures growing from one point in all three directions, but they may be the result of lateral linkage of several folds growing towards each other (Grasemann and Schmalholz, 2012; Bretis et al., 2011). Such fold linkage can lead to crooked fold hinges that do not align with the theoretical fold axis orientation. Second, the influence of basement structures in the NW ZSFB is not clear. Folds may develop above basement faults as fault-propagation folds or fault-bend folds. In this case, the fold orientation is inherited from the basement structure, which does not necessarily follow the theoretical fold axis orientation.

## 5. Conclusions

The presented numerical models of 3D fold growth in transpression show that the rate of fold growth is significantly different for different convergence angles. In all three directions, the fold growth rate increases with increasing convergence angle (i.e., folds grow faster in pure shear than in simple shear). Despite the different rates, the general growth behavior is very similar for different convergence angles (see also Frehner (2014) for pure shear). For all convergence angles, the two lateral fold growth rates are similar, resulting in a lateral fold aspect ratio close to 1; hence the bulk fold structure occupies a continuously growing roughly circular area. The orientation of the fold axis is always parallel to the major horizontal principal strain axis,  $\vec{\lambda}_{\max}$ , independent of convergence angle and viscosity ratio, confirming the findings of Tikoff and Peterson (1998); the fold initiates in this direction and rotates to stay parallel to this orientation. In other words, the fold hinge is not a passive line fixed to the material; hinge migration takes place as a consequence.

There is a triangular relationship between convergence angle, amount of strain, and fold axis orientation, which is independent of viscosity ratio. In natural situations, this relationship can be used to estimate one of these values if the other two are known. On a large scale, strain in transpression may be partitioned (Jones and Tanner, 1995) between simple-shear dominated (e.g., strike-slip faults) and pure-shear dominated systems (e.g., fold-and-thrust belt). Therefore, the convergence angle associated with folding may be significantly smaller than the obliquity of the background convergence (which may be known from GPS measurements). Fold axis orientations in transpressional systems may be assumed parallel to the orientation of the major horizontal principal strain axis and the fold amplitudes in all three directions may be used to estimate the background strain. With this information, the above-mentioned triangular relationship can be used to estimate the convergence angle associated with the observed fold structures and hence infer the strain partitioning ratio.

## Acknowledgements

The valuable reviews of Peter Hudleston and Boris Kaus helped improve an earlier version of the manuscript. Helpful discussions with and comments from Neil S. Mancktelow are also greatly acknowledged. This work was supported by the ETH Zurich, Switzerland.

## Appendix A. Continuum mechanics equations

Buckle folding is assumed to be a slow flow process governed by incompressible Newtonian (linear viscous) rheology. The continuum

mechanics equations describing such flow behavior comprise the conservation of linear momentum (i.e., force balance),

$$\begin{aligned} \frac{\partial \sigma_{xx}}{\partial x} + \frac{\partial \sigma_{xy}}{\partial y} + \frac{\partial \sigma_{xz}}{\partial z} &= 0 \\ \frac{\partial \sigma_{yx}}{\partial x} + \frac{\partial \sigma_{yy}}{\partial y} + \frac{\partial \sigma_{yz}}{\partial z} &= 0, \\ \frac{\partial \sigma_{zx}}{\partial x} + \frac{\partial \sigma_{zy}}{\partial y} + \frac{\partial \sigma_{zz}}{\partial z} &= 0 \end{aligned} \quad (A1)$$

the conservation of angular momentum, expressed as

$$\sigma_{ij} = \sigma_{ji}, \quad (A2)$$

the rheological (constitutive) equation,

$$\sigma_{ij} = 2\eta \dot{\epsilon}_{ij} - \delta_{ij} \left( p + 2\eta \frac{\dot{\epsilon}_{xx} + \dot{\epsilon}_{yy} + \dot{\epsilon}_{zz}}{3} \right), \quad (A3)$$

the kinematical relationship,

$$\dot{\epsilon}_{ij} = \frac{1}{2} \left( \frac{\partial v_i}{\partial j} + \frac{\partial v_j}{\partial i} \right), \quad (A4)$$

and the incompressibility condition (vanishing divergence of the velocity field),

$$\frac{\partial v_x}{\partial x} + \frac{\partial v_y}{\partial y} + \frac{\partial v_z}{\partial z} = 0. \quad (A5)$$

In Eqs. (A1)–(A5),  $\sigma_{ij}$  are the six independent components of the stress tensor,  $x$ ,  $y$ , and  $z$  are the three Cartesian coordinate directions (Fig. 1),  $\eta$  is the dynamic viscosity,  $\dot{\epsilon}_{ij}$  are the six independent components of the strain rate tensor,  $\delta_{ij}$  is the Kronecker delta,  $p$  is the pressure (i.e., negative mean normal stress), and  $v_x$ ,  $v_y$ , and  $v_z$  are the three components of the velocity vector. Subscripts  $i$  and  $j$  do not imply Einstein summation but are placeholders for  $x$ ,  $y$ , and  $z$ . Note that in Eq. (A1) no gravity and no inertia terms are used and that Eq. (A3) represents a linear relationship between stress and strain rate (i.e., Newtonian rheology).

## Appendix B. Numerical finite-element method

Eqs. (A1)–(A5) are discretized using the finite-element (FE) method. The particular self-developed numerical code has been introduced in Frehner (2014) and corresponds to a 3D-extension of the 2D codes explained and benchmarked in Frehner and Schmalholz (2006), Frehner (2011), and Frehner and Exner (2014). An equivalent code has been used in Schmalholz (2008) and Reber et al. (2010).

Discretization is done by applying a Galerkin approach on a mixed velocity–pressure–penalty formulation of the continuum mechanics equations (Hughes, 2000). The penalty approach is coupled with an Uzawa-type iteration (Pelletier et al., 1989) to ensure incompressibility. The numerical Lagrangian (i.e., deformable) grid consists of isoparametric hexahedral Q27/4-elements (Zienkiewicz and Taylor, 2000) with continuous quadratic shape functions for the velocity degrees of freedom and discontinuous linear shape functions for the pressure degrees of freedom. The numerical grid is set up in such a way that physical interfaces do not cross elements; hence no interpolation is necessary. In other words, interfaces between different material phases (two layers in the presented cases) coincide with element boundaries. A numerical integration scheme on 27 Gauss-Legendre quadrature points (Bathe, 1996) without any remeshing has been found to be sufficient for the relatively small strains obtained in the presented simulations. The code has successfully been benchmarked against the analytical thick-plate folding solution of Fletcher (1991).

### Appendix C. Measures for applied background strains

For general transpression, there is no unique measure for the applied bulk strain suitable for all convergence angles. Fossen et al. (2013) proposed two different measures: the lengths of the minor ( $|\vec{\lambda}_{\min}|$ ) and major ( $|\vec{\lambda}_{\max}|$ ) horizontal principal strain axes, respectively (see Figs. 4 and 7 in Fossen et al. (2013)). The first is a suitable global measure valid for all convergence angles (Fig. A1a); it may be translated to an effective bulk shortening as  $\varepsilon_{\min} = 1 - |\vec{\lambda}_{\min}|$ . Equivalently,  $|\vec{\lambda}_{\max}|$  may be translated to an effective bulk extension as  $\varepsilon_{\max} = |\vec{\lambda}_{\max}| - 1$ .

However, the latter remains constant during deformation for a convergence angle of  $\alpha = 90^\circ$  (pure shear, Fig. A1b); hence it does not qualify as a global strain measure. A more suitable measure for the applied bulk strain may be the strain axis ratio,

$$R_\lambda = \frac{|\vec{\lambda}_{\max}|}{|\vec{\lambda}_{\min}|}. \quad (\text{C1})$$

For the relatively small strains obtained in this study and for the different convergence angles,  $R_\lambda$  develops almost identically to the pure-shear case (Fig. A1c), namely

$$R_\lambda \approx \exp(t\dot{\varepsilon}_{\text{bg}}), \quad (\text{C2})$$

which would make it an obvious choice for measuring the global bulk strain. However, the drawback is that a certain strain axis ratio does not reveal if it is due to an increase of  $|\vec{\lambda}_{\max}|$  or a decrease of  $|\vec{\lambda}_{\min}|$ .

Another possibility is to use the pure-shear component (in y-direction) of the bulk strain given as

$$\varepsilon_{\text{ps}} = 1 - \exp[-\sin(\alpha)t\dot{\varepsilon}_{\text{bg}}]. \quad (\text{C3})$$

The drawback of this measure is that for a convergence angle of  $\alpha = 0^\circ$  (simple shear) it remains zero during deformation (Fig. A1d). Alternatively, the simple-shear component of the bulk strain may be used, given as the shear angle

$$\psi = \tan^{-1}[\cos(\alpha)t\dot{\varepsilon}_{\text{bg}}]. \quad (\text{C4})$$

Similar to above, the drawback of this measure is that for a convergence angle of  $\alpha = 90^\circ$  (pure shear) it remains zero during deformation (Fig. A1e). However, for the relatively small strains obtained in the presented simulations, Eq. (C3) for pure shear (i.e.,  $\sin(\alpha = 90^\circ) = 1$ ) and Eq. (C4) for simple shear (i.e.,  $\cos(\alpha = 0^\circ) = 1$ ) yield almost identical

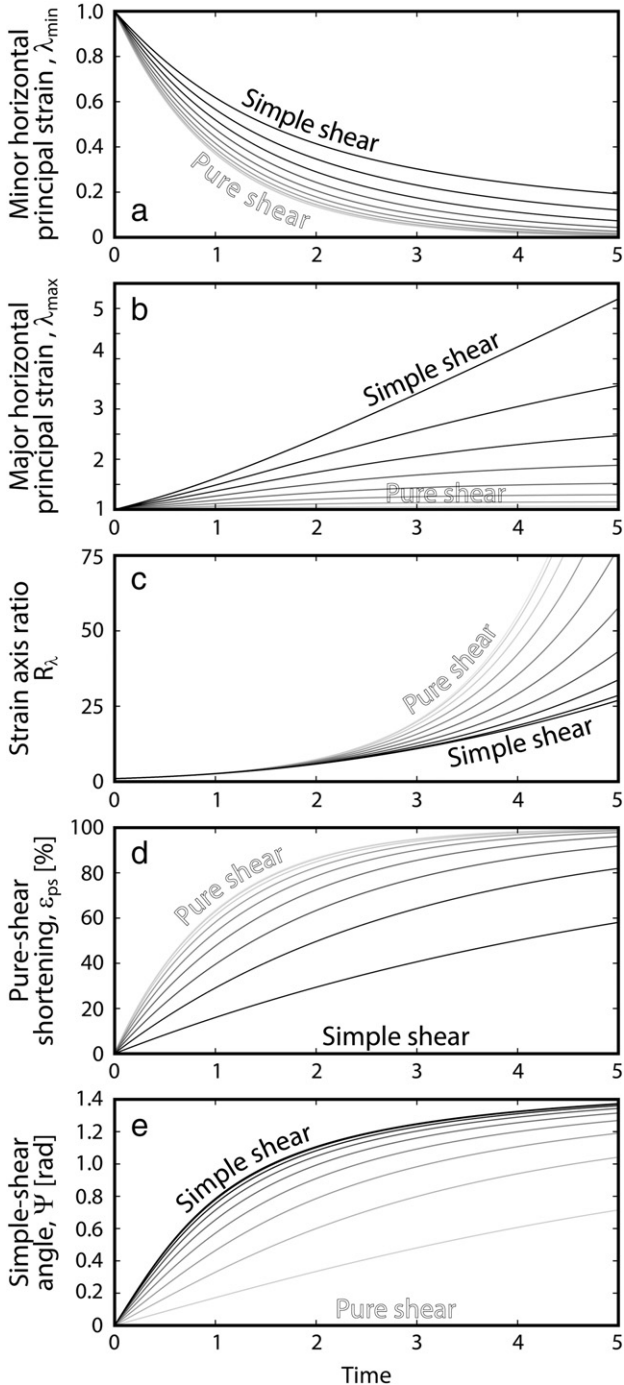


Fig. A1. Various strain measures plotted versus progressive time for different convergence angles from  $0^\circ$  (simple shear) to  $90^\circ$  (pure shear).

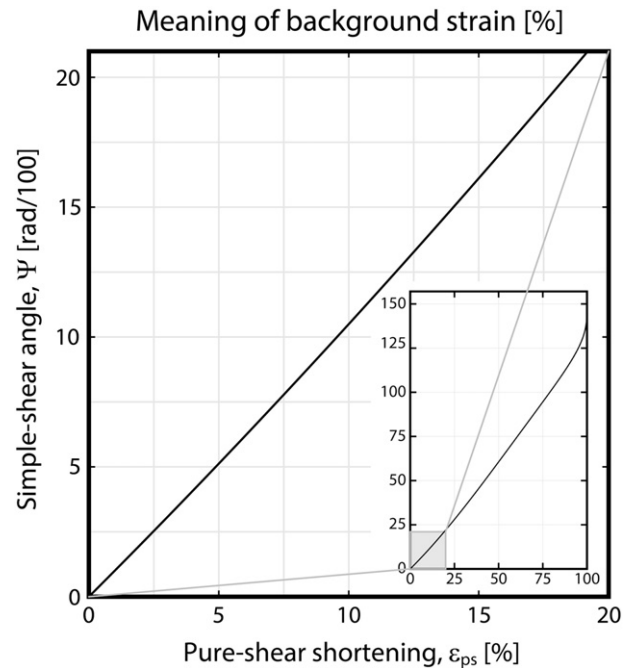


Fig. A2. Simple-shear angle,  $\Psi$  (Eq. (C4)), for simple shear ( $\alpha = 0^\circ$ ) plotted versus pure-shear shortening component,  $\varepsilon_{\text{ps}}$  (Eq. (C3)) for pure shear ( $\alpha = 90^\circ$ ). The inset shows the entire spectrum of possible values; the main figure shows the range of strains obtained in this study, for which the two measures are almost identical.

values (Fig. A2). Therefore, the global background strain measure for all convergence angles is proposed here as

$$\epsilon_{bg} = 1 - \exp(-t\dot{\epsilon}_{bg}), \quad (C5)$$

where the background strain rate,  $\dot{\epsilon}_{bg}$ , is a pre-defined value (i.e.,  $\dot{\epsilon}_{bg} = 1$ ).

## References

- Abbassi, M.R., Mancktelow, N.S., 1992. Single layer buckle folding in non-linear materials—I. Experimental study of fold development from an isolated initial perturbation. *J. Struct. Geol.* 14, 85–104. [http://dx.doi.org/10.1016/0191-8141\(92\)90147-0](http://dx.doi.org/10.1016/0191-8141(92)90147-0).
- Bathe, K.-J., 1996. *Finite Element Procedures*. Prentice Hall, Englewood Cliffs.
- Biot, M.A., 1961. Theory of folding of stratified viscoelastic media and its implications in tectonics and orogenesis. *Geol. Soc. Am. Bull.* 72, 1595–1620. [http://dx.doi.org/10.1130/0016-7606\(1961\)72\[1595:TOFOSV\]2.0.CO;2](http://dx.doi.org/10.1130/0016-7606(1961)72[1595:TOFOSV]2.0.CO;2).
- Bobyarchick, A.R., 1986. The eigenvalues of steady flow in Mohr space. *Tectonophysics* 122, 35–51. [http://dx.doi.org/10.1016/0040-1951\(86\)90157-5](http://dx.doi.org/10.1016/0040-1951(86)90157-5).
- Bretis, B., Bartl, N., Grasemann, B., 2011. Lateral fold growth and linkage in the Zagros fold and thrust belt (Kurdistan, NE Iraq). *Basin Res.* 23, 615–630. <http://dx.doi.org/10.1111/j.1365-2117.2011.00506.x>.
- Casas, A.M., Gapais, D., Nalpas, T., Besnard, K., Román-Berdiel, T., 2001. Analogue models of transpressive systems. *J. Struct. Geol.* 23, 733–743. [http://dx.doi.org/10.1016/S0191-8141\(00\)00153-X](http://dx.doi.org/10.1016/S0191-8141(00)00153-X).
- Collignon, M., Kaus, B.J.P., May, D.A., Fernandez, N., 2014. Influences of surface processes on fold growth during 3-D detachment folding. *Geochem. Geophys. Geosyst.* 15, 3281–3303. <http://dx.doi.org/10.1002/2014GC005450>.
- Dewey, J.F., Holdsworth, R.E., Strachan, R.A., 1998. Transpression and transtension zones. *Geol. Soc. Lond., Spec. Publ.* 135, 1–14. <http://dx.doi.org/10.1144/GSL.SP.1998.135.01.01>.
- Fernandez, N., Kaus, B.J.P., 2014. Fold interaction and wavelength selection in 3D models of multilayer detachment folding. *Tectonophysics* 632, 199–217. <http://dx.doi.org/10.1016/j.tecto.2014.06.013>.
- Fletcher, R.C., 1977. Folding of a single viscous layer: exact infinitesimal-amplitude solution. *Tectonophysics* 39, 593–606. [http://dx.doi.org/10.1016/0040-1951\(77\)90155-X](http://dx.doi.org/10.1016/0040-1951(77)90155-X).
- Fletcher, R.C., 1991. Three-dimensional folding of an embedded viscous layer in pure shear. *J. Struct. Geol.* 13, 87–96. [http://dx.doi.org/10.1016/0191-8141\(91\)90103-P](http://dx.doi.org/10.1016/0191-8141(91)90103-P).
- Fletcher, R.C., 1995. Three-dimensional folding and necking of a power-law layer: are folds cylindrical, and, if so, do we understand why? *Tectonophysics* 247, 65–83. [http://dx.doi.org/10.1016/0040-1951\(95\)00021-E](http://dx.doi.org/10.1016/0040-1951(95)00021-E).
- Fossen, H., Tikoff, B., 1993. The deformation matrix for simultaneous simple shearing, pure shearing and volume change, and its application to transpression-transension tectonics. *J. Struct. Geol.* 15, 413–422. [http://dx.doi.org/10.1016/0191-8141\(93\)90137-Y](http://dx.doi.org/10.1016/0191-8141(93)90137-Y).
- Fossen, H., Teysier, C., Whitney, D.L., 2013. Transtensional folding. *J. Struct. Geol.* 56, 89–102. <http://dx.doi.org/10.1016/j.jsg.2013.09.004>.
- Frehner, M., 2011. The neutral lines in buckle folds. *J. Struct. Geol.* 33, 1501–1508. <http://dx.doi.org/10.1016/j.jsg.2011.07.005>.
- Frehner, M., 2014. 3D fold growth rates. *Terra Nova* 26, 417–424. <http://dx.doi.org/10.1111/ter.12116>.
- Frehner, M., Exner, U., 2014. Strain and foliation refraction patterns around buckle folds. *Geol. Soc. Lond., Spec. Publ.* 394, 21–37. <http://dx.doi.org/10.1144/SP394.4>.
- Frehner, M., Schmalholz, S.M., 2006. Numerical simulations of parasitic folding in multilayers. *J. Struct. Geol.* 28, 1647–1657. <http://dx.doi.org/10.1016/j.jsg.2006.05.008>.
- Frehner, M., Exner, U., Mancktelow, N.S., Grujic, D., 2011. The not-so-simple effects of boundary conditions on models of simple shear. *Geology* 39, 719–722. <http://dx.doi.org/10.1130/G31957.1>.
- Frehner, M., Reif, D., Grasemann, B., 2012. Mechanical versus kinematical shortening reconstructions of the Zagros High Folded Zone (Kurdistan region of Iraq). *Tectonics* 31. <http://dx.doi.org/10.1029/2011TC003010> (TC3002).
- Ghosh, S.K., 1970. A theoretical study of intersecting fold patterns. *Tectonophysics* 9, 559–569. [http://dx.doi.org/10.1016/0040-1951\(70\)90006-5](http://dx.doi.org/10.1016/0040-1951(70)90006-5).
- Ghosh, N., Chakra, M., Chattopadhyay, A., 2014. An experimental approach to strain pattern and folding in unconfined and/or partitioned transpressional deformation. *Int. J. Earth Sci.* 103, 349–365. <http://dx.doi.org/10.1007/s00531-013-0951-z>.
- Grasemann, B., Schmalholz, S.M., 2012. Lateral fold growth and fold linkage. *Geology* 40, 1039–1042. <http://dx.doi.org/10.1130/G33613.1>.
- Grujic, D., Mancktelow, N.S., 1995. Folds with axes parallel to the extension direction: an experimental study. *J. Struct. Geol.* 17, 279–291. [http://dx.doi.org/10.1016/0191-8141\(94\)E0048-4](http://dx.doi.org/10.1016/0191-8141(94)E0048-4).
- Hughes, T.J.R., 2000. *The Finite Element Method: Linear Static and Dynamic Finite Element Analysis*. Dover Publications, Mineola.
- Jackson, J., 1992. Partitioning of strike-slip and convergent motion between Eurasia and Arabia in eastern Turkey and the Caucasus. *J. Geophys. Res.* 97, 12471–12479. <http://dx.doi.org/10.1029/92JB00944>.
- James, A.I., Watkinson, A.J., 1994. Initiation of folding and boudinage in wrench shear and transpression. *J. Struct. Geol.* 16, 883–893. [http://dx.doi.org/10.1016/0191-8141\(94\)90152-X](http://dx.doi.org/10.1016/0191-8141(94)90152-X).
- Jones, R.R., Tanner, P.W.G., 1995. Strain partitioning in transpression zones. *J. Struct. Geol.* 17, 793–802. [http://dx.doi.org/10.1016/0191-8141\(94\)00102-6](http://dx.doi.org/10.1016/0191-8141(94)00102-6).
- Kaus, B.J.P., Schmalholz, S.M., 2006. 3D finite amplitude folding: Implications for stress evolution during crustal and lithospheric deformation. *Geophys. Res. Lett.* 33, L14309. <http://dx.doi.org/10.1029/2006GL026341>.
- Kellogg, K.S., Minor, S.A., 2005. Pliocene transpressional modification of depositional basins by convergent thrusting adjacent to the “Big Bend” of the San Andreas fault: An example from Lockwood Valley, southern California. *Tectonics* 24, TC1004. <http://dx.doi.org/10.1029/2003TC001610>.
- Leever, K.A., Gabrielsen, R.H., Faleide, J.I., Braathen, A., 2011. A transpressional origin for the West Spitsbergen fold-and-thrust belt: Insight from analog modeling. *Tectonics* 30, TC2014. <http://dx.doi.org/10.1029/2010TC002753>.
- Lupi, M., Miller, S.A., 2014. Short-lived tectonic switch mechanism for long-term pulses of volcanic activity after mega-thrust earthquakes. *Solid Earth* 5, 13–24. <http://dx.doi.org/10.5194/se-5-13-2014>.
- Masson, F., Chéry, J., Hatzfeld, D., Martinod, J., Vernant, P., Tavakoli, F., Ghafari-Ashtiany, M., 2005. Seismic versus aseismic deformation in Iran inferred from earthquakes and geodetic data. *Geophys. J. Int.* 160, 217–226. <http://dx.doi.org/10.1111/j.1365-246X.2004.02465.x>.
- Mohajjel, M., Fergusson, C.L., 2000. Dextral transpression in Late Cretaceous continental collision, Sanandaj–Sirjan Zone, western Iran. *J. Struct. Geol.* 22, 1125–1139. [http://dx.doi.org/10.1016/S0191-8141\(00\)00023-7](http://dx.doi.org/10.1016/S0191-8141(00)00023-7).
- Mühlhaus, H.-B., Sakaguchi, H., Hobbs, B.E., 1998. Evolution of three-dimensional folds for a non-Newtonian plate in a viscous medium. *Proc. R. Soc. A – Math. Phys. Eng. Sci.* 454, 3121–3143. <http://dx.doi.org/10.1098/rspa.1998.0294>.
- Payrola, P.A., Hongn, F., Cristallini, E., García, V., del Papa, C., 2012. Andean oblique folds in the Cordillera Oriental – Northwestern Argentina: Insights from analogue models. *J. Struct. Geol.* 42, 194–211. <http://dx.doi.org/10.1016/j.jsg.2012.05.003>.
- Pelletier, D., Fortin, A., Camarero, R., 1989. Are FEM solutions of incompressible flows really incompressible? (or how simple flows can cause headaches!). *Int. J. Numer. Methods Fluids* 9, 99–112. <http://dx.doi.org/10.1002/flid.1650090108>.
- Reber, J.E., Schmalholz, S.M., Burg, J.-P., 2010. Stress orientation and fracturing during three-dimensional buckling: Numerical simulation and application to chocolate-tablet structures in folded turbidites, SW Portugal. *Tectonophysics* 493, 187–195. <http://dx.doi.org/10.1016/j.tecto.2010.07.016>.
- Reif, D., Grasemann, B., Faber, R.H., 2011. Quantitative structural analysis using remote sensing data: Kurdistan, northeast Iraq. *AAPG Bull.* 95, 941–956. <http://dx.doi.org/10.1306/11151010112>.
- Reif, D., Grasemann, B., Peresson, H., 2012. Fracture patterns in the Zagros fold-and-thrust belt, Kurdistan Region of Iraq. *Tectonophysics* 576–577, 46–62. <http://dx.doi.org/10.1016/j.tecto.2012.07.024>.
- Robin, P., Cruden, A.R., 1994. Strain and vorticity patterns in ideally ductile transpression zones. *J. Struct. Geol.* 16, 447–466. [http://dx.doi.org/10.1016/0191-8141\(94\)90090-6](http://dx.doi.org/10.1016/0191-8141(94)90090-6).
- Sanderson, D.J., Marchini, W.R.D., 1984. Transpression. *J. Struct. Geol.* 6, 449–458. [http://dx.doi.org/10.1016/0191-8141\(84\)90058-0](http://dx.doi.org/10.1016/0191-8141(84)90058-0).
- Sarkarinejad, K., 2007. Quantitative finite strain and kinematic flow analyses along the Zagros transpression zone, Iran. *Tectonophysics* 442, 49–65. <http://dx.doi.org/10.1016/j.tecto.2007.04.007>.
- Schmalholz, S.M., 2006. Finite amplitude folding of single layers: elastica, bifurcation and structural softening. *Philos. Mag.* 86, 3393–3407. <http://dx.doi.org/10.1080/14786430500197785>.
- Schmalholz, S.M., 2008. 3D numerical modeling of forward folding and reverse unfolding of a viscous single-layer: Implications for the formation of folds and fold patterns. *Tectonophysics* 446, 31–41. <http://dx.doi.org/10.1016/j.tecto.2007.09.005>.
- Schmalholz, S.M., Podladchikov, Y.Y., Burg, J.-P., 2002. Control of folding by gravity and matrix thickness: Implications for large-scale folding. *J. Geophys. Res.* 107, 2005. <http://dx.doi.org/10.1029/2001JB000355>.
- Schmid, D.W., Dabrowski, M., Krotkiewski, M., 2008. Evolution of large amplitude 3D fold patterns: A FEM study. *Phys. Earth Planet. Inter.* 171, 400–408. <http://dx.doi.org/10.1016/j.pepi.2008.08.007>.
- Simpson, G., 2004. Role of river incision in enhancing deformation. *Geology* 32, 341–344. <http://dx.doi.org/10.1130/G20190.1>.
- Talebani, M., Jackson, J., 2002. Offset on the Main Recent Fault of NW Iran and implications for the late Cenozoic tectonics of the Arabia–Eurasia collision zone. *Geophys. J. Int.* 150, 422–439. <http://dx.doi.org/10.1046/j.1365-246X.2002.01711.x>.
- Talebani, M., Jackson, J., 2004. A reappraisal of earthquake focal mechanisms and active shortening in the Zagros mountains of Iran. *Geophys. J. Int.* 156, 506–526. <http://dx.doi.org/10.1111/j.1365-246X.2004.02092.x>.
- Teyssier, C., Tikoff, B., Markley, M., 1995. Oblique plate motion and continental tectonics. *Geology* 23, 447. [http://dx.doi.org/10.1130/0091-7613\(1995\)023<0447:OPMACT>2.3.CO;2](http://dx.doi.org/10.1130/0091-7613(1995)023<0447:OPMACT>2.3.CO;2).
- Tikoff, B., Peterson, K., 1998. Physical experiments of transpressional folding. *J. Struct. Geol.* 20, 661–672. [http://dx.doi.org/10.1016/S0191-8141\(98\)00004-2](http://dx.doi.org/10.1016/S0191-8141(98)00004-2).
- Tikoff, B., Teysier, C., 1994. Strain modeling of displacement-field partitioning in transpressional orogens. *J. Struct. Geol.* 16, 1575–1588. [http://dx.doi.org/10.1016/0191-8141\(94\)90034-5](http://dx.doi.org/10.1016/0191-8141(94)90034-5).
- Toy, V.G., Norris, R.J., Prior, D.J., Walrond, M., Cooper, A.F., 2013. How do lineations reflect the strain history of transpressive shear zones? The example of the active Alpine Fault zone, New Zealand. *J. Struct. Geol.* 50, 187–198. <http://dx.doi.org/10.1016/j.jsg.2012.06.006>.
- Treagus, J.E., Treagus, S.H., 1981. Folds and the strain ellipsoid: a general model. *J. Struct. Geol.* 3, 1–17. [http://dx.doi.org/10.1016/0191-8141\(81\)90052-3](http://dx.doi.org/10.1016/0191-8141(81)90052-3).
- Venkat-Ramani, M., Tikoff, B., 2002. Physical models of transtensional folding. *Geology* 30, 523. [http://dx.doi.org/10.1130/0091-7613\(2002\)030<0523:PMOTF>2.0.CO;2](http://dx.doi.org/10.1130/0091-7613(2002)030<0523:PMOTF>2.0.CO;2).
- Vernant, P., Chéry, J., 2006. Mechanical modelling of oblique convergence in the Zagros, Iran. *Geophys. J. Int.* 165, 991–1002. <http://dx.doi.org/10.1111/j.1365-246X.2006.02900.x>.
- Yamato, P., Kaus, B.J.P., Mouthereau, F., Castelltort, S., 2011. Dynamic constraints on the crustal-scale rheology of the Zagros fold belt, Iran. *Geology* 39, 815–818. <http://dx.doi.org/10.1130/G32136.1>.

Zebari, M.M., Burberry, C.M., 2015. 4-D evolution of anticlines and implications for hydrocarbon exploration within the Zagros Fold-Thrust Belt, Kurdistan Region, Iraq. *GeoArabia* 20, 161–188.

Zienkiewicz, O.C., Taylor, R.L., 2000. *The Finite Element Method, Volume 1: The Basis*. Butterworth-Heinemann, Oxford.

Zulauf, G., Zulauf, J., Hastreiter, P., Tomandl, B., 2003. A deformation apparatus for three-dimensional coaxial deformation and its application to rheologically stratified analogue material. *J. Struct. Geol.* 25, 469–480. [http://dx.doi.org/10.1016/S0191-8141\(02\)00023-8](http://dx.doi.org/10.1016/S0191-8141(02)00023-8).